eScience 2 (2022) 192–200

Contents lists available at ScienceDirect

eScience

journal homepage: www.keaipublishing.com/en/journals/escience

Research Paper

Electroactive polymeric nanofibrous composite to drive in situ construction of lithiophilic SEI for stable lithium metal anodes

Ai-Long Chen [a], Nan Shang [a], Yue Ouyang [a], Lulu Mo [a], Chunyang Zhou [a], Weng Weei Tjiu [d], Feili Lai [c], Yue-E Miao [a,*], Tianxi Liu [a,b,*]

[a] State Key Laboratory for Modification of Chemical Fibers and Polymer Materials, College of Materials Science and Engineering, Donghua University, Shanghai, 201620, PR China
[b] Key Laboratory of Synthetic and Biological Colloids, Ministry of Education, School of Chemical and Material Engineering, Jiangnan University, Wuxi, 214122, PR China
[c] Department of Chemistry, KU Leuven, Celestijnenlaan 200F, Leuven, 3001, Belgium
[d] Institute of Materials Research and Engineering, Agency for Science, Technology and Research (A*STAR), 2 Fusionopolis Way, 138634, Singapore

HIGHLIGHTS

- A novel lithium-ion flux distributor derived from an electroactive polymeric composite nanofiber interlayer is proposed.
- The PVDF/PMMA composite interlayer achieved uniform lithium nucleation at molecular level and dendrite-free deposition.
- The corresponding Li || $LiFePO_4$ full cell presents a high rate capacity of 110 mAh g^{-1} at 10 C.

GRAPHICAL ABSTRACT

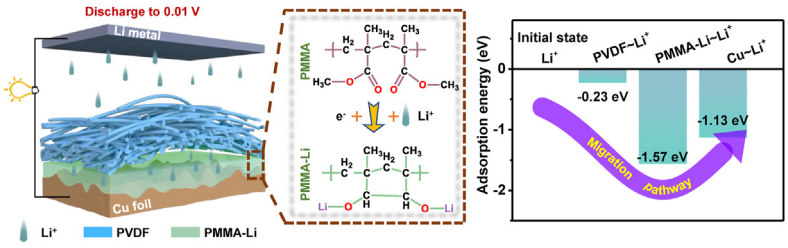

ARTICLE INFO

Keywords:
Electroactive polymer nanofibers
Electrospinning
Li^+ flux regulation
Dendrite-free
Lithium metal battery

ABSTRACT

Uncontrolled lithium dendrite growth hinders the practical application of lithium metal batteries (LMBs). Herein, we report a novel Li^+ flux distributor achieved by placing an electroactive polyvinylidene fluoride/polymethyl methacrylate (PVDF/PMMA) composite nanofiber interlayer on a current collector, inducing uniform lithium deposition to mitigate the dendrite problem. Specifically, the released PMMA reacts with Li^+ to form abundant C–O–Li bonds and generate in situ a stable lithiophilic PMMA-Li solid electrolyte interphase layer. Theoretical calculations reveal that polar C–F groups in the PVDF framework and lithiophilic PMMA-Li provide homo-dispersed Li^+ migration pathways with low energy barriers. Consequently, uniform Li nucleation is achieved at the molecular level, resulting in ultrahigh cycling stability with dendrite-free Li deposition at 5 mA cm^{-2} and 5 mAh cm^{-2} for over 500 h. The PVDF/PMMA ~ Li || $LiFePO_4$ (LFP) full cell presents an increased rate capacity of 110 mAh g^{-1} at 10 C. In addition, a soft-package battery demonstrates a high energy density of 289 Wh kg^{-1}. This work provides a facile design for stable lithium metal anodes to promote the practical use of LMBs and other alkali metal batteries.

1. Introduction

The rapid development of electric vehicles and portable electronics has increased the demand for batteries with high energy density, long cycle life, and good safety [1,2]. Conventional lithium-ion batteries struggle to meet these criteria, due to their limited practical energy

* Corresponding authors.
E-mail addresses: yuee_miao@dhu.edu.cn (Y.-E. Miao), txliu@dhu.edu.cn (T. Liu).

https://doi.org/10.1016/j.esci.2022.02.003
Received 1 November 2021; Received in revised form 21 December 2021; Accepted 14 February 2022
Available online 18 February 2022

density (usually $\leq$ 250 Wh kg^{-1}) [3]. However, the lithium metal anode has high volumetric and gravimetric specific capacities of 2046 mAh cm^{-3} and 3860 mAh g^{-1}, as well as the lowest reported reduction potential (−3.04 V vs. standard hydrogen electrode), making it an ideal candidate for high-energy-density lithium metal batteries (LMBs), such as lithium-sulfur and lithium-air batteries [4–7]. Nevertheless, the development of LMBs still faces many challenges, including inhomogeneous lithium deposition arising from a nonuniform solid electrolyte interphase (SEI) layer [8]. In addition, the huge volume expansion that lithium metal undergoes destroys the native SEI and results in abundant lithium dendrites. In severe cases, it can even puncture the separator and lead to a short circuit and thermal runaway [9–14]. It therefore is essential to prevent the uneven deposition of lithium metal to achieve stable, safe LMBs.

Much effort has been devoted to addressing the above problems of lithium metal anodes. Intrinsically, an even SEI is the foundation for inducing uniform lithium-ion (Li^+) flux at the lithium metal surface; this can be effectively realized through physico-chemical modifications of the SEI to regulate the current distribution during Li deposition [15]. Various electrolyte additives have been used [16–20], as well as artificial protective layers [21–25], to form a stable SEI and prevent the accumulation of Li^+ at "hot spots" [26–30]. Although remarkable progress has been achieved in the regulation of Li deposition behaviors, these SEIs are too brittle to withstand the large volume changes that lithium metal undergoes. Relative to other methods, designing interfacial layers is a promising option to address the dendrite growth issue, as these layers have high strength and do not consume electrolyte during long-term cycling [31–33]. However, without the buffering and blocking effect of a compact SEI, lithium metal still will easily grow into the interlayer and render it useless [34]. Hence, it is of vital importance to construct a compact, stable protective layer to manipulate Li^+ distribution during the long-term cycling process.

Polar functional groups within interlayers have been demonstrated to have a strong affinity toward Li^+ in the electrolyte and to guide uniform Li^+ flux distribution on the electrode [5,34], thereby reducing the rate of Li^+ accumulation at "hot spots" [35–37]. Herein, we report a robust polyvinylidene fluoride/polymethyl methacrylate (PVDF/PMMA) composite nanofiber membrane fabricated by a facile electrospinning method, which can be applied as a three-dimensional (3D) electroactive interlayer to achieve homogeneous Li^+ flux and dendrite-free lithium deposition in LMBs. Both theoretical calculations and experimental results demonstrate that the PVDF nanofiber framework with polar C–F groups acts not only as a highly porous carrier for PMMA but also as a 3D interconnected protective network for the compact SEI during long-term cycling. The electroactive PMMA molecules released from the composite fibers react with Li^+ to develop abundant C–O–Li bonds and in situ generate a lithiophilic PMMA-Li SEI layer on Cu foil, which helps deposit the allocated Li^+ flux evenly to achieve uniform Li nucleation at the molecular level. Benefiting from smooth, dense, and dendrite-free lithium deposition, a symmetric cell with a PVDF/PMMA interlayer exhibits excellent cycle life for more than 500 h, and an ultralow polarization of ~30 mV under a high current density of 5 mA cm^{-2} and a deposition capacity of 5 mAh cm^{-2}. When coupled in a Li || LFP full cell, a modified battery with a PVDF/PMMA interlayer also exhibits outstanding cycling stability and rate capability. The stable electrochemical performance contributed by the hierarchical regulation of uniform Li^+ flux paves the way for eliminating lithium dendrites in future practical high-energy LMB applications.

2. Results and discussion

2.1. Materials design and characterization

Fig. 1a schematically illustrates the electrospinning process used to generate the PVDF/PMMA composite nanofiber interlayer, as well as the protective barriers provided for the lithium metal anode by the 3D PVDF nanofiber framework and the PMMA-Li SEI layer constructed in situ. Through regulation of the collection time, the PVDF/PMMA composite nanofiber membrane had a uniform fiber diameter of ~300 nm with a controlled thickness of ~30 μm (Figs. 1b and c). The PVDF and PVDF/PMMA membranes also demonstrated excellent affinity for the electrolyte, yielding a contact angle of 0° (Figs. 1d and S1), which is attributed to their high porosity and uniform pore size distributions of 0.76 μm and 0.88 μm, respectively (Fig. S2). In particular, the good affinity between Li^+ and the highly polar C–F groups in PVDF improved the interfacial compatibility between the PVDF/PMMA interlayer and the electrodes, thereby significantly enhancing Li^+ transport efficiency during cycling (Fig. S3 and Table S1).

The Fourier transform infrared (FTIR) spectrum of PVDF/PMMA showed a typical absorption peak at about 1403.2 cm^{-1} (Figs. 1e and S4), assigned to the bending vibration peak of the CH_2 group connected to the CF_2 group in PVDF. The stretching vibration peak at 1179.5 cm^{-1} is assigned to the CF_2 in PVDF, and the peak at 1728.8 cm^{-1} indicates the C═O stretching vibration of PMMA. The PVDF/PMMA composite interlayer is a critical component for safe battery operation; notably, thermal gravimetric analysis (TGA) indicated it exhibited good thermal stability, with gradual weight loss occurring only above 220 °C (Figs. 1f and S5). Furthermore, the PVDF/PMMA composite nanofiber membrane showed excellent mechanical performance, with a high tensile strength of 55.98 MPa (Fig. 1g), guaranteeing its integrity and stability after the in situ formation of PMMA-Li SEI as a protective barrier.

To track the Li^+ migration pathway through the PVDF/PMMA composite interlayer to the Cu foil, density functional theory (DFT) calculations were conducted to analyze the adsorption energy values of Li^+ on different functional groups. As shown in Fig. 2a, the PMMA-Li exhibited the most negative adsorption energy toward Li^+ (−1.57 eV), compared with C–F (−0.23 eV) and the Cu (111) surface (−1.13 eV), indicating that Li^+ was preferentially adsorbed by PMMA-Li during the migration process and thermodynamically facilitated the uniform nucleation of lithium metal at the molecular level. This indicated a low-energy Li^+ migration pathway from the Li anode to the Cu foil, driven by the strong adsorption energy of the PVDF/PMMA composite interlayer toward Li^+ (Fig. 2b).

To further investigate the conversion mechanism of PMMA molecules on the electrode, Li–Cu half cells were assembled with pristine Cu foil and using PVDF or PVDF/PMMA as a protective interlayer. The cyclic voltammetry (CV) curves in Fig. S6 show no distinct peaks for the cell using bare Cu foil. In comparison, the CV curve of the cell with the PVDF/PMMA interlayer presents two obvious reduction peaks at 1.20 V and 0.61 V, while an anodic peak appears at 1.14 V during the first cycle. The marked reduction peak around 1.20 V that nearly disappears in the second cycle is closely associated with the first-step reaction of Li^+ and PMMA, appearing in the first cycle only to form PMMA-Li. The discharge curve of the cell with PVDF/PMMA (Fig. 2c) also exhibits two small plateaus, around 1.12 V and 0.55 V, corresponding to the two-step reactions of PMMA molecules upon lithium plating to form PMMA═O and PMMA-Li, respectively.

To further clarify the reaction mechanisms of PMMA during the lithium deposition process, FTIR analyses of the Cu foil in different discharge states were carried out, as displayed in Fig. 2d. The C–O–C vibration peaks at 1149 cm^{-1} and the C═O stretch mode peaks at 1735 cm^{-1} are attributed to the ester carbonyl group in PMMA [38,39]. After discharging to 0.01 V in the first cycle, these two peaks were completely replaced by three new vibration peaks at 1650, 1080, and ~530 cm^{-1}, belonging to the keto carbonyl group, C–O, and Li–O vibrations, respectively, originating from PMMA-Li [40–42]. When the battery was recharged to 0.5 V, the peak intensity of C–O and Li–O decreased, demonstrating a reversible transition from PMMA-Li into PMMA═O during the stripping process.

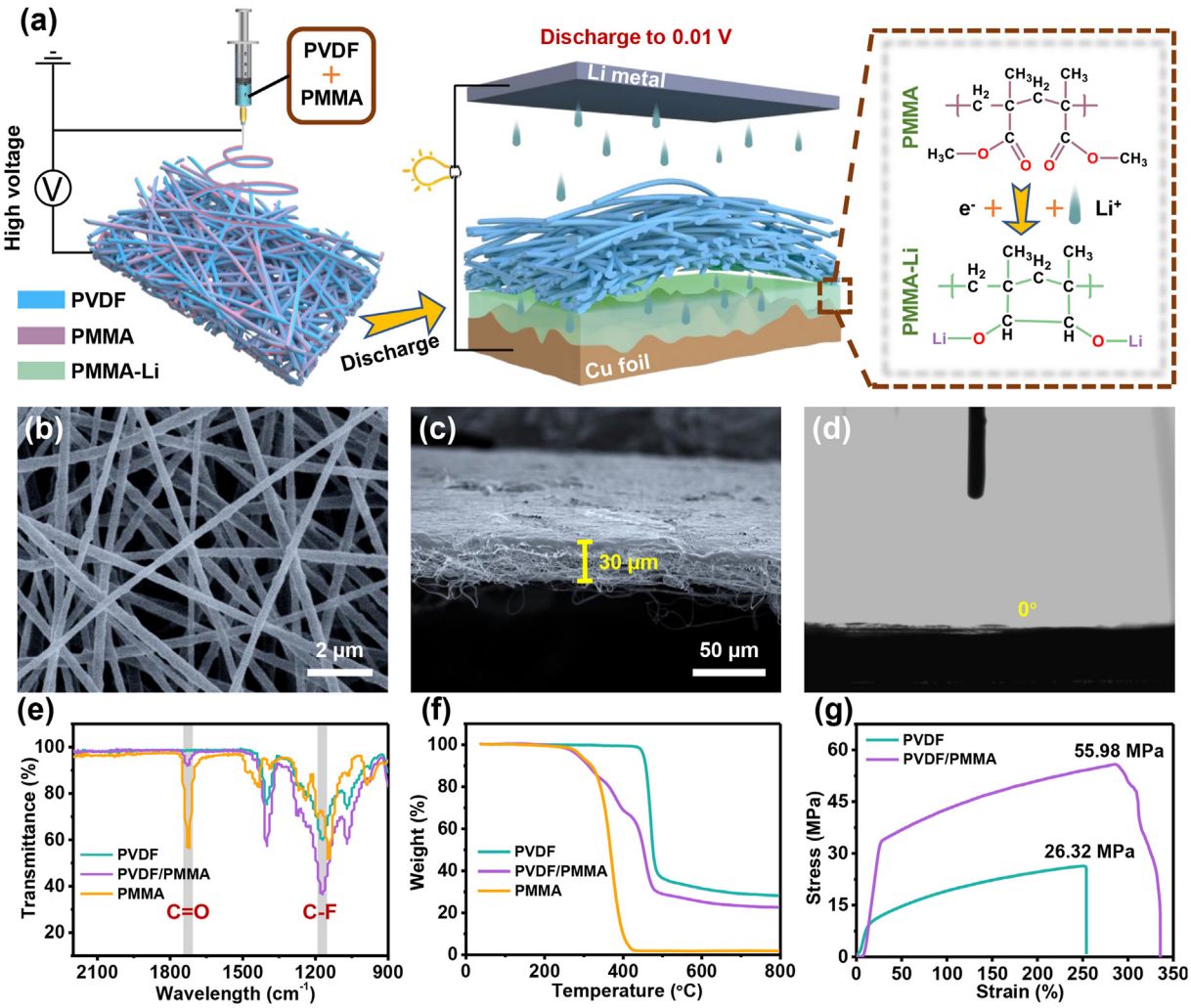

Fig. 1. (a) Schematic illustration of the fabrication of PVDF/PMMA nanofiber membrane and its application as an electroactive protective interlayer in LMBs. (b) Top-view and (c) cross-sectional SEM images, and (d) the electrolyte contact angle of the PVDF/PMMA membrane. (e) FTIR spectra and (f) TGA curves of PVDF, PMMA, and PVDF/PMMA membranes. (g) The Young's modulus of PVDF and PVDF/PMMA membranes.

To further demonstrate the precise structural evolution of PMMA during the charge/discharge process, ex situ XPS analysis was performed to investigate the surface composition of SEI before and after discharging. After discharging to 0.01 V, the characteristic peaks at 288.6 eV and 286.3 eV, corresponding to the ester carbonyl carbon (O═C–O) and methoxyl carbon (O–CH_3) [43–45], disappeared, while a new peak for keto carbonyl carbon (O═C) was observed at 289.9 eV in the fitted C 1s spectra (Figs. S7a and b). Also after discharging, the peaks of methoxyl oxygen (C–O–CH_3, 533.3 eV) and ester carbonyl oxygen (O═C–O, 531.7 eV) were replaced by two new peaks for keto carbonyl oxygen (531.9 eV) and the C–O–Li bond (542 eV) in the fitted O 1s spectra (Figs. S7c and d) [44,46,47]. The FTIR and XPS results, which are in agreement, offer strong proof of the fast reaction kinetics that the PVDF/PMMA interlayer provides in the formation of the uniform PMMA-Li SEI, which promoted even Li^+ flux distribution and homogeneous lithium deposition on the current collector after receiving electrons.

COMSOL Multiphysics theoretical simulations were used to reveal spatial distributions and dynamic change processes in the well-designed model systems with/without PVDF/PMMA composite protective interlayers, to intuitively present the Li^+ flux and E-field distributions within a whole battery (Figs. 3a, b and Fig. S8). Typically, bare Cu foil without any protection readily led to severe aggregation of Li^+ flux at the locally high current density bump (Figs. 3c, d and g), causing the nonuniform deposition of lithium metal during the plating process (Movie S1). After the PVDF nanofiber membrane was incorporated, more homogeneous Li^+ flux distribution and lithium plating were achieved, which was attributed to the porous structure of the PVDF nanofiber membrane (Figs. 3e, h and Movie S2). Notably, the plating process under the PVDF/PMMA-Li protective interlayer showed an even distribution of Li^+ flux, with almost no curvatures on the surface of the Cu foil (Figs. 3f and i). Hence, smooth, dense deposition was obtained even after 1000 s of plating (Movie S3 and Fig. S9). The even Li^+ flux effectively suppressed the potential difference inside the battery by incorporating PVDF/PMMA, which efficiently diminished the electric field polarization along the electrode surface (Figs. S10 and S11). The theoretical simulations provided a comprehensive understanding of precisely how the PVDF/PMMA composite interlayer regulated Li^+ flux distribution and lithium deposition behaviors.

Supplementary data related to this article can be found at https://doi.org/10.1016/j.esci.2022.02.003.

2.2. *Electrochemical performance of PVDF/PMMA-incorporated cells*

To benefit from the homogenized Li^+ flux, Cu foil was directly applied as a current collector and assembled with the PVDF/PMMA composite

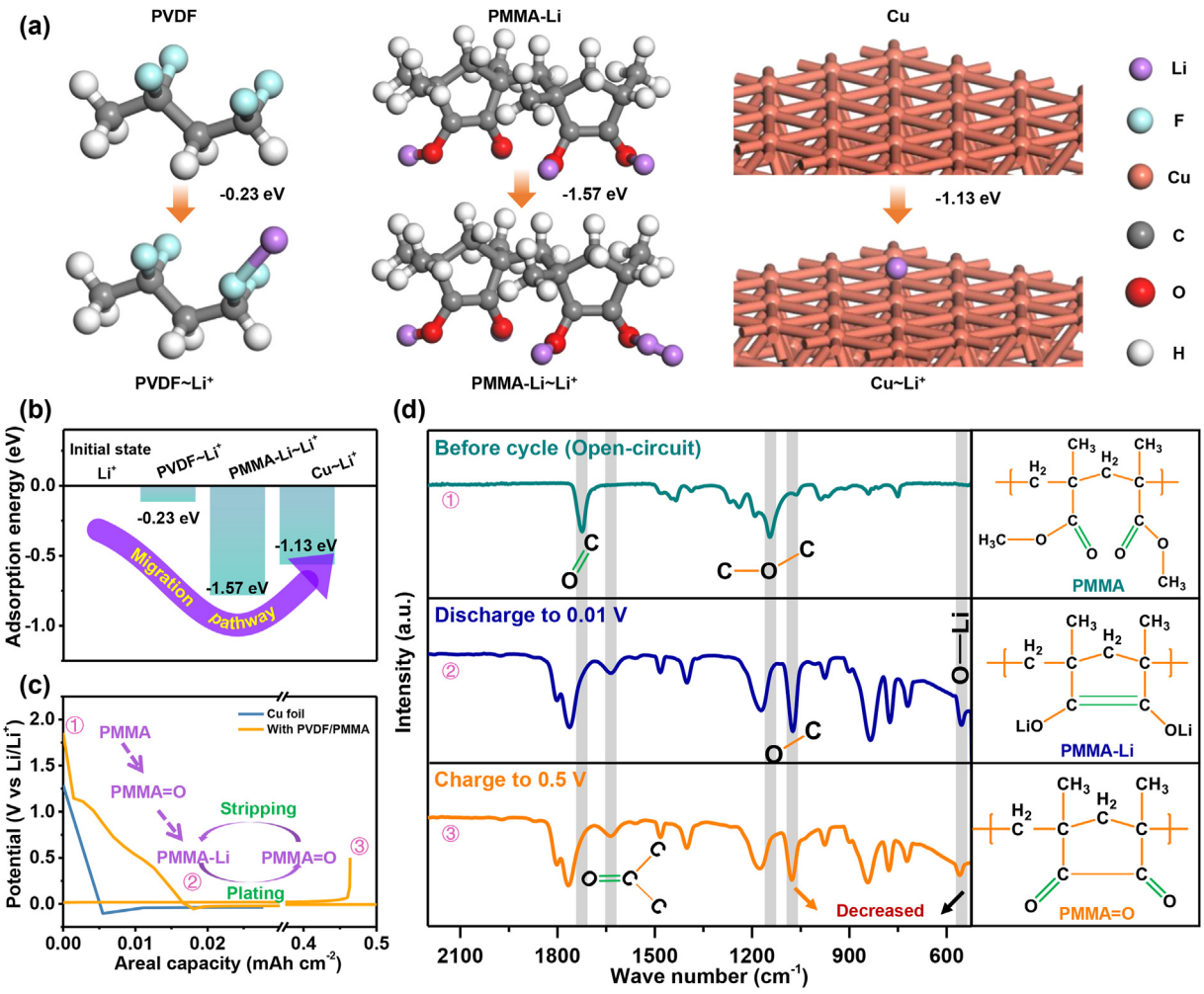

Fig. 2. (a) Theoretical calculation of the adsorption energy after coordination with Li^+ upon simplified fragments of PVDF, PMMA-Li, and Cu foil with a (111) plane. (b) The migration pathway and corresponding energy barrier for Li^+ diffusion through the PVDF/PMMA interlayer. (c) The initial discharge curves of Li–Cu half cells with bare Cu foil and the PVDF/PMMA interlayer. (d) The FTIR spectra obtained over the Cu foil surface at different stages, with the corresponding molecular structures of PMMA.

interlayer to accommodate Li metal under a high capacity of 10 mAh cm^{-2} at 1.0 mA cm^{-2}. Li dendrites several micrometers in size were loosely deposited on the bare Cu foil surface (Figs. 4a and b). This undesired morphology was attributed to the nonuniform Li^+ flux distribution in the electrolyte and the "tip effect" caused by defects on the Cu foil surface (Fig. 4c). When the PVDF nanofiber framework was introduced, larger, evenly distributed lithium particles with cracks were observed on the Cu foil surface (Figs. 4d and e). Nonetheless, the PVDF nanofiber interlayer was insufficient to thoroughly homogenize the Li deposition, due to the preferred aggregation of the Li^+ flux around the "hot spot" of Cu foil under higher current densities (Fig. 4f). Notably, fairly flat, dense Li deposition was achieved, without dendritic formation, using the PVDF/PMMA composite interlayer (Figs. 4g and h). The apparent morphological difference indicated that the PMMA-Li SEI formed in situ further guided the uniform transport of the immobilized Li^+ to the current collector surface and facilitated the even nucleation of lithium metal at the molecular level (Fig. 4i).

The suppression of Li dendrites by the PVDF/PMMA composite was thoroughly investigated using Li–Cu half-cells, as illustrated in Fig. 5. The nucleation overpotentials were obtained from the voltage–capacity profiles at a current density of 0.5 mA cm^{-2} (Fig. 5a). The Li–Cu cell with a PVDF/PMMA interlayer exhibited a much lower nucleation overpotential (6 mV) than the cells with a PVDF interlayer (25 mV) or bare Cu foil (59 mV). This was ascribed to the reduced nucleation resistance of lithium metal on the Cu foil due to the in situ formation of an ultra-lithiophilic PMMA-Li SEI layer.

Electrochemical impedance spectroscopy (EIS) analyses before and after 50 cycles of Li plating/stripping were conducted at 0.5 mA cm^{-2} with a cycling capacity of 1.0 mAh cm^{-2} to further investigate the interfacial stability. As shown in Fig. 5b and Fig. S12, the cell with bare Cu foil had a large interfacial resistance of 46 Ω before cycling, which dropped to 23.5 Ω after 50 cycles. In comparison, the cell with the PVDF/PMMA interlayer exhibited a relatively lower interfacial resistance of 22 Ω before cycling and only 2.6 Ω after 50 cycles, which was also demonstrated by the low voltage hysteresis and steady capacity retention in the voltage profiles for different cycles (Fig. S13). These results indicated that the PVDF/PMMA interlayer provided a very stable SEI layer and efficiently promoted the charge transfer kinetics during the cycling process of lithium plating/stripping.

Coulombic efficiency (CE), defined as the ratio of Li stripping capacity to Li deposition capacity for each cycle, is a critical index for evaluating the reversibility of a lithium metal anode in relation to SEI formation and dendrite growth. As shown in Fig. 5c, at a constant current density of 0.5 mA cm^{-2} and a capacity of 1.0 mAh cm^{-2}, the CE of the bare Cu foil-based cell rapidly decayed to 59.3% after only 180 cycles, owing to the formation of "dead lithium" stemming from the irreversible breaking away of the fragile dendrites. After a PVDF interlayer was introduced, the cycling stability of the Li–Cu half-cell was better, but it still became

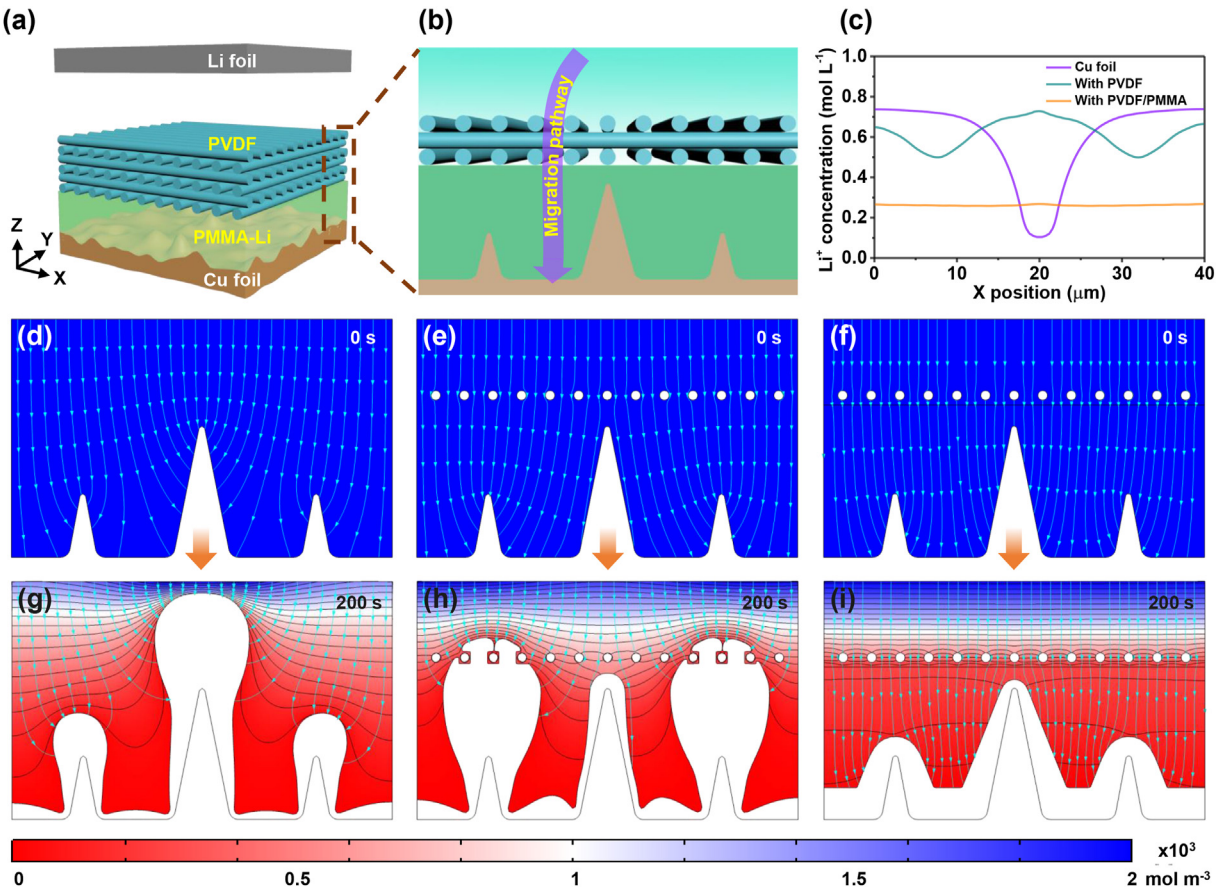

Fig. 3. (a) COMSOL simulation illustrations of a PVDF/PMMA-based half-cell system. (b) Migration pathway, illustrating Li^+ diffusion through the PVDF/PMMA composite nanofiber interlayer. (c) Li^+ concentration distributions along the X direction. The COMSOL simulation cell geometry for the anode (d–f) before lithium deposition and (g–i) after deposition for 200 s; (d, g) with bare Cu foil, and protected by (e, h) PVDF interlayer or (f, i) PVDF/PMMA interlayer. The black line is the isoconcentration line in the electrolyte, and the cyan arrow indicates the direction and size of Li^+ flux.

unstable after 230 cycles. In sharp contrast, the cycle life of the Li–Cu half-cell modified with the PVDF/PMMA interlayer was much longer (320 cycles), with a stable CE that decayed only slightly to 98.6%; this was a better result than has been reported in many previous studies that used differently designed interlayers (Table S2). When the current density was increased to 1.0 mA cm^{-2}, all of the modified Li–Cu half-cells with different PVDF/PMMA interlayers showed significantly better cycling stability than the half-cell with bare Cu foil (Fig. S14). With an optimal mass ratio between the PVDF and PMMA components, the modified Li–Cu half-cell maintained a relatively stable CE of 97.8% for more than 200 cycles under 1.0 mA cm^{-2} and 1 mAh cm^{-2}, while the cell with bare Cu foil suffered sudden failure after only 60 cycles (Fig. S15a). When the deposition capacity was further increased to 2 mAh cm^{-2}, the Li–Cu half-cell containing the PVDF/PMMA interlayer circulated stably for 100 cycles at a high CE of 97.7% (Fig. S15b). The excellent electrochemical performance derived mainly from the significantly enhanced interfacial stability and effective suppression of dendritic lithium, stemming from the dual functions of the PVDF distributor and the PMMA-driven SEI.

The two-electrode symmetric cells were cycled using a galvanostatic method to evaluate the long-term cycling stability at various current densities. Fig. 5d and Fig. S16 show the voltage profiles of the symmetric cells with bare Li foil and different interlayers at 1 mA cm^{-2} under a fixed stripping/plating capacity of 1 mAh cm^{-2}. The symmetric cell assembled with pristine Li displayed a gradually higher overpotential up to 300 mV after only 360 h, indicating an unstable Li–electrolyte interface due to the formation of "dead lithium." With the PVDF interlayer, the symmetric cell exhibited enhanced cycling stability but a very high polarization voltage. In comparison, the battery with the PVDF/PMMA interlayer delivered an ultralow voltage hysteresis of 25 mV over 550 cycles without drastic fluctuation (Fig. 5e), which was superior to previously reported findings (Table S3). At an even higher current density of 2 mA cm^{-2}, the symmetric cell with the PVDF/PMMA interlayer still stayed stable for over 850 h with a low hysteresis (Fig. S17). However, the pristine Li electrode without any protective layers displayed gradually greater hysteresis. The short-circuit phenomenon appeared earlier for pristine Li at the higher current density of 5 mA cm^{-2} (Fig. 5f). Notably, the symmetric cell with the PVDF/PMMA interlayer still performed well beyond 500 h, with a stable voltage overpotential, and maintained the lowest voltage hysteresis even at a high current density of 10 mA cm^{-2} (Fig. 5g), reconfirming the important role of the 3D PVDF/PMMA nanofibrous interlayer in guiding the uniform distribution of Li^+ flux and the electric field. The stable long-term cycling performance was also brought about by the small interfacial resistance of the symmetric cell protected with the PVDF/PMMA interlayer after cycling (Fig. S18).

Remarkably, the deposition morphologies of the Li anodes in different symmetric cells after 50 cycles intuitively proved the superiority of PVDF/PMMA during the plating/stripping process (Fig. S19). The Li anode protected with the PVDF/PMMA composite interlayer maintained a smooth, flat surface without any obvious dendrites. With respect to the morphology of the interlayers after cycling, the PVDF/PMMA nanofibers maintained a smooth, fibrous structure, even though the PMMA component participated reversibly in the plating/stripping process (Fig. S20a). However, there were several "dead lithium" residues on the PVDF interlayer, due to the growth of lithium dendrites into the interlayer (Fig. S20b).

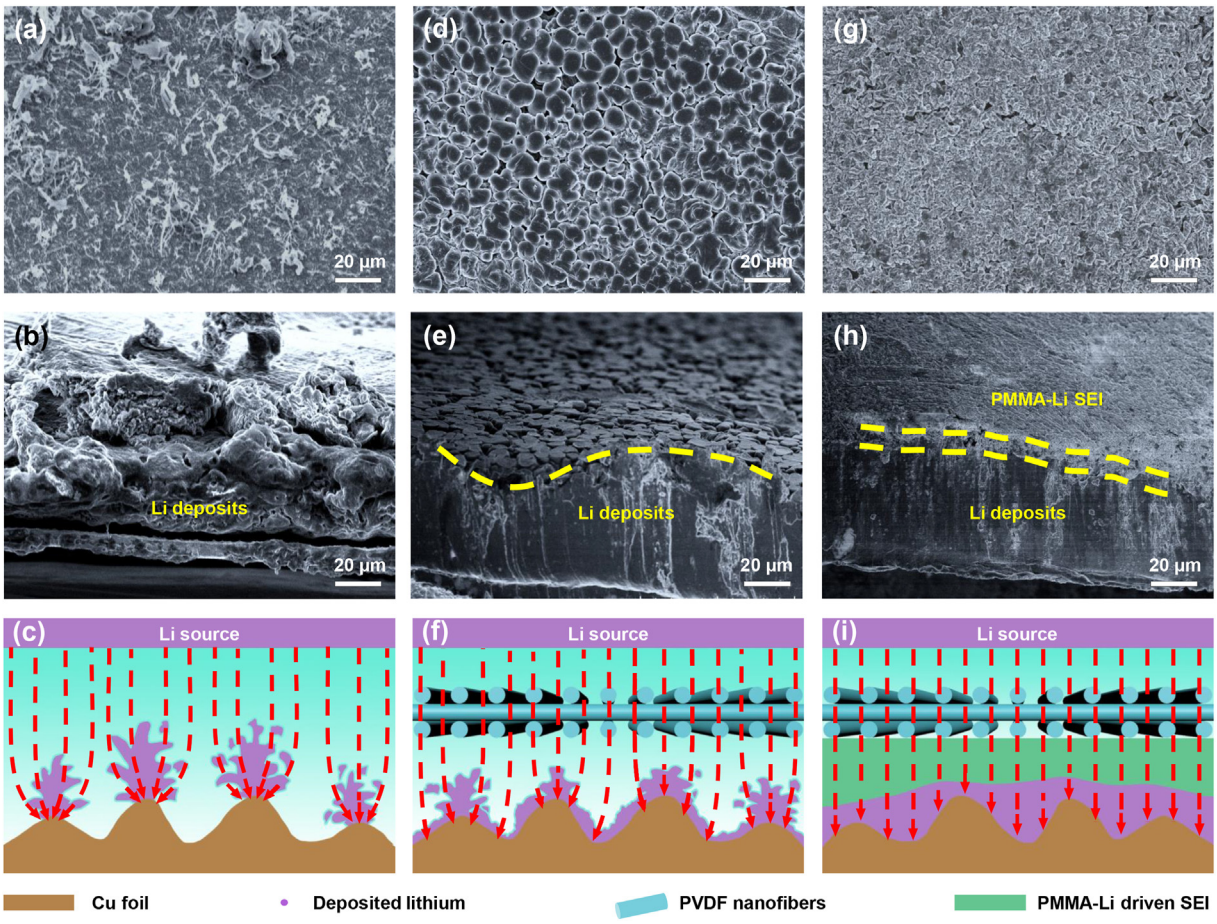

Fig. 4. SEM images and nucleation schematic diagrams showing the morphology of Li deposits (a–c) on bare Cu foil, and Cu foils in batteries with (d–f) PVDF and (g–i) PVDF/PMMA interlayers under 10 mAh cm^{-2} and 1 mA cm^{-2}.

Finally, the PVDF and PVDF/PMMA interlayers were coupled in full cells with a Li foil anode and a $LiFePO_4$ (LFP) cathode to demonstrate their use in practical applications. The full-cell rate capability from 0.5 C to 10 C is presented in Figs. 6a–d. At a low rate of 0.5 C, the discharge capacity, CE, and voltage hysteresis values for the three types of full cells showed small differences. However, at the gradually increased rate of 10 C, the bare Li || LFP full cell showed a severely decayed capacity of only 60 mAh g^{-1} and a dramatic increase in the voltage hysteresis of 293 mV. With its stabilized interface and uniform Li plating/stripping process, the PVDF/PMMA ~ Li || LFP full cell maintained a more stable discharge capacity of up to 108 mAh g^{-1}, accompanied by a lower voltage hysteresis of 200 mV.

The long-term cycling performance and CE of the full cells at 1 C are shown in Fig. 6e. Impressively, the PVDF/PMMA ~ Li || LFP full cell retained a high discharge specific capacity of up to 120 mAh g^{-1}, even after 400 cycles (Fig. S21). Further, a high CE value of over 99.6% was maintained during the entire cycling life. This emphatically demonstrated that the protective PVDF/PMMA interlayer on the Li anode extended the cycling life of the full cells. In addition, the PVDF/PMMA interlayer ran stably in a high-voltage PVDF/PMMA~Li || NCM811 battery (Fig. S22). A 7 Ah soft-package battery with a capacity of 6.75 Ah and a total weight of 74.66 g even realized a high energy density of up to 289 Wh kg^{-1} (444 Wh L^{-1}) (Figs. 6f–h and Fig. S23), further extending the practicality of the PVDF/PMMA composite nanofiber interlayer for stabilizing the SEI formed in situ and the high-energy lithium metal anode.

3. Conclusion

In summary, we have successfully manipulated the deposition behavior of Li metal with a simple PVDF/PMMA composite nanofiber interlayer obtained by the electrospinning method. Both theoretical simulations and experimental results proved that the PVDF nanofiber network, containing a large number of polar C–F groups, homogenized the Li^+ flux in the electrolyte, while the PMMA released in situ reacted with Li^+ to form a lithiophilic PMMA-Li SEI layer. As a result, both uniform Li^+ flux distribution and dense Li nucleation were achieved at the molecular level. The symmetric cell protected by a PVDF/PMMA interlayer presented an ultralong lifespan of more than 500 h at a current density of 5 mA cm^{-2} and an areal capacity of 5 mAh cm^{-2}. At the same time, the PVDF/PMMA ~ Li || LFP full cell exhibited a greatly enhanced capacity of up to 120 mAh g^{-1} at a rate of 1 C after 400 cycles. The PVDF/PMMA ~ Li || LFP soft-package battery further demonstrated a practical energy density of up to 289 Wh kg^{-1}. We believe that the twofold induction described here offers a promising strategy for bringing highly stable, dendrite-free lithium metal batteries to the energy industry.

4. Experimental section

4.1. Materials

N,N-Dimethylformamide (DMF) was supplied by Shanghai Macklin Biochemical Co., Ltd. Polyvinylidene fluoride (PVDF, $M_w = 950{,}000$) and polymethyl methacrylate (PMMA, $M_w = 960{,}000$) were provided by Arkema Co., Ltd. Ketjen black was purchased from DoDoChem Co., Ltd. All the chemicals were used without further purification.

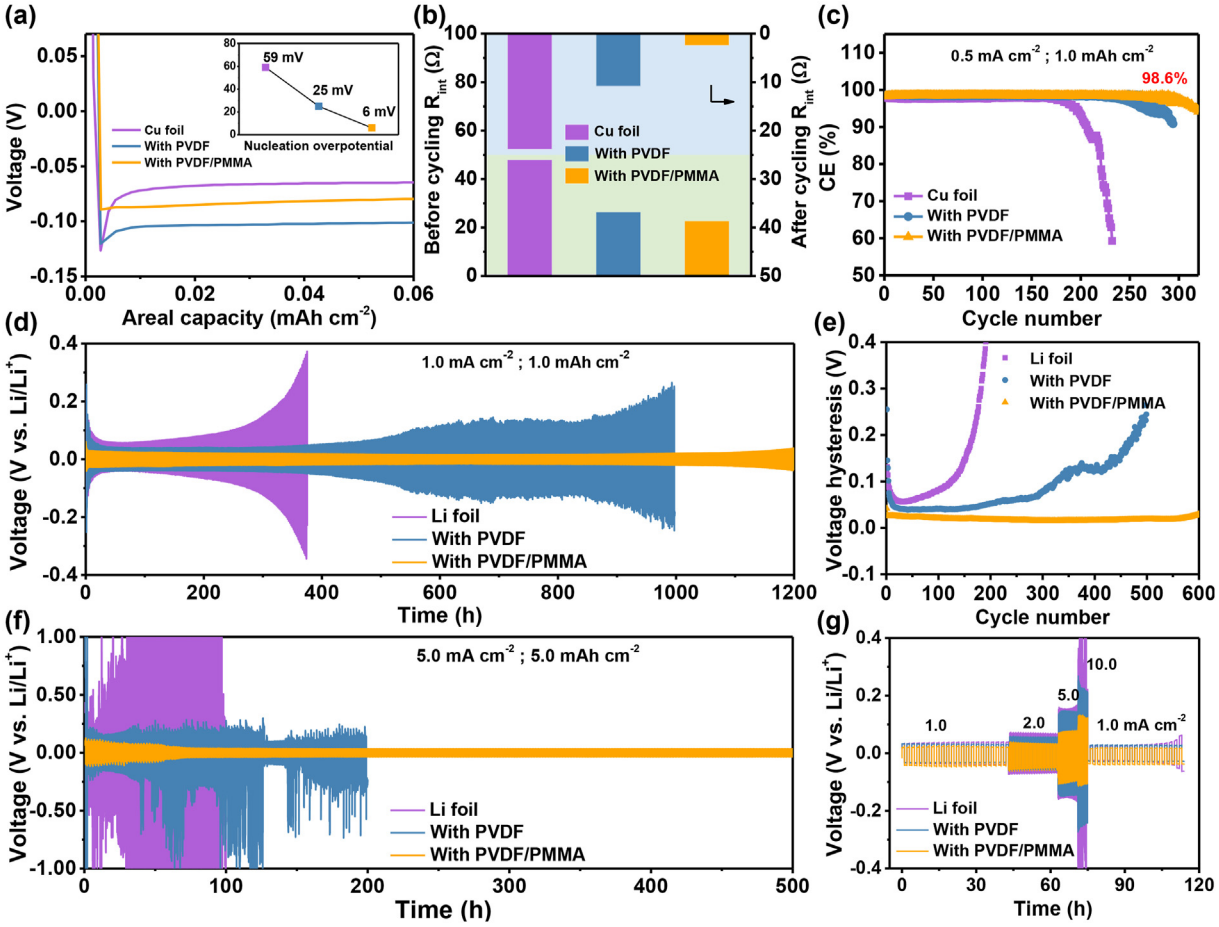

Fig. 5. (a) The nucleation overpotential and (b) interfacial impedance of Li–Cu half cells with bare Cu foil, PVDF, and PVDF/PMMA interlayers before and after 50 cycles. (c) The coulombic efficiency of Li–Cu half cells with different protective layers, cycled at 0.5 mA cm^{-2} with a cycling capacity of 1.0 mAh cm^{-2}. Voltage profiles at a current density of (d) 1.0 mA cm^{-2} under 1.0 mAh cm^{-2}, and (f) 5 mA cm^{-2} under 5 mAh cm^{-2}; and (e) the corresponding average voltage hysteresis of Li–Li symmetric cells. (g) Rate capability profiles of the Li–Li symmetric cells.

4.2. Preparation of electrospun PVDF/PMMA composite nanofiber membranes

The spinning solution was obtained by dissolving the PVDF and PMMA in DMF solvent in a mass ratio of 2:1 with vigorous stirring at room temperature for 12 h. Then, 3 mL of the above prepared homogeneous transparent solution was transferred into a 5 mL syringe for electrospinning. The electrospinning process was carried out at room temperature (25 ± 2 °C) and a constant ambient moisture of 30 ± 3%. A constant voltage of 15 kV was used, with the syringe at a fixed feeding rate (0.08 mm min^{-1}). The distance between the rotating aluminum foil collector and the syringe tip was locked at 15 cm. Eventually, the as-prepared nanofiber membrane was transferred to a high-temperature oven at 60 °C for 15 h to completely evaporate the solvent and obtain the composite membrane, which was designated $PVDF_2/PMMA_1$.

For comparison, pure PVDF, PMMA, and PVDF/PMMA composite nanofabrics with different weight ratios of PVDF to PMMA (8:1, 4:1, and 1:1) were also prepared by the same procedure and were denoted as PVDF, PMMA, $PVDF_8/PMMA_1$, $PVDF_4/PMMA_1$, and $PVDF_1/PMMA_1$.

4.3. Characterization

The surface morphology of the various samples was observed using a field emission scanning electron microscope (FE-SEM, JEOL, 7500F, Japan). The electrolyte affinities of the interlayers were investigated with a contact angle analyzer (OSA200, Germany). The mechanical performance was characterized via a universal testing machine (UTM2102, Shenzhen Suns Technology Stock Co., Ltd, China) using a 6 mm min^{-1} stretching speed. FTIR was applied to characterize the chemical structure of the membrane surface using a NEXUS-670 FTIR spectroscope (Thermo Nicolet, USA). The thermal stability was studied with a thermal gravimetric analyzer (TG 209 F1 Libra) from 30 to 800 °C under a N_2 atmosphere at a heating rate of 10 °C min^{-1}.

4.4. Electrochemical tests

Evaluation of the electrochemical performance was carried out in coin cells (CR2025) using a Li metal disk as the counter electrode. The cell assembly process was conducted in a glove box filled with Ar. In all coin cells, 60 μL of 1.0 M LiTFSI in DOL/DME (1:1 by volume) with 2 wt% $LiNO_3$ was used as the electrolyte, and a Celgard 2500 separator was placed between the two electrodes. Then, the above-prepared membranes were cut into circular pellets (16 mm in diameter) and placed between the separator and the current collectors.

To compare the Li nucleation overpotential and CE during the plating/stripping process, Li–Cu half-cells were assembled. The cutoff potential was fixed at 0.5 V during the Li stripping process. The symmetric cell was assembled with two Li foils and a PVDF/PMMA-sandwiched Celgard separator. A CHI660E electrochemical workstation was used to investigate the EIS of the symmetric cells (the frequency range was fixed at 0.1–10^5 Hz). The ionic conductivity (σ) was tested in a symmetric stainless steel (SS)/SS cell at room temperature. A cut-off voltage window of 0.01–3 V was set during the CV analysis process, and the scan rate was 1 mV s^{-1}.

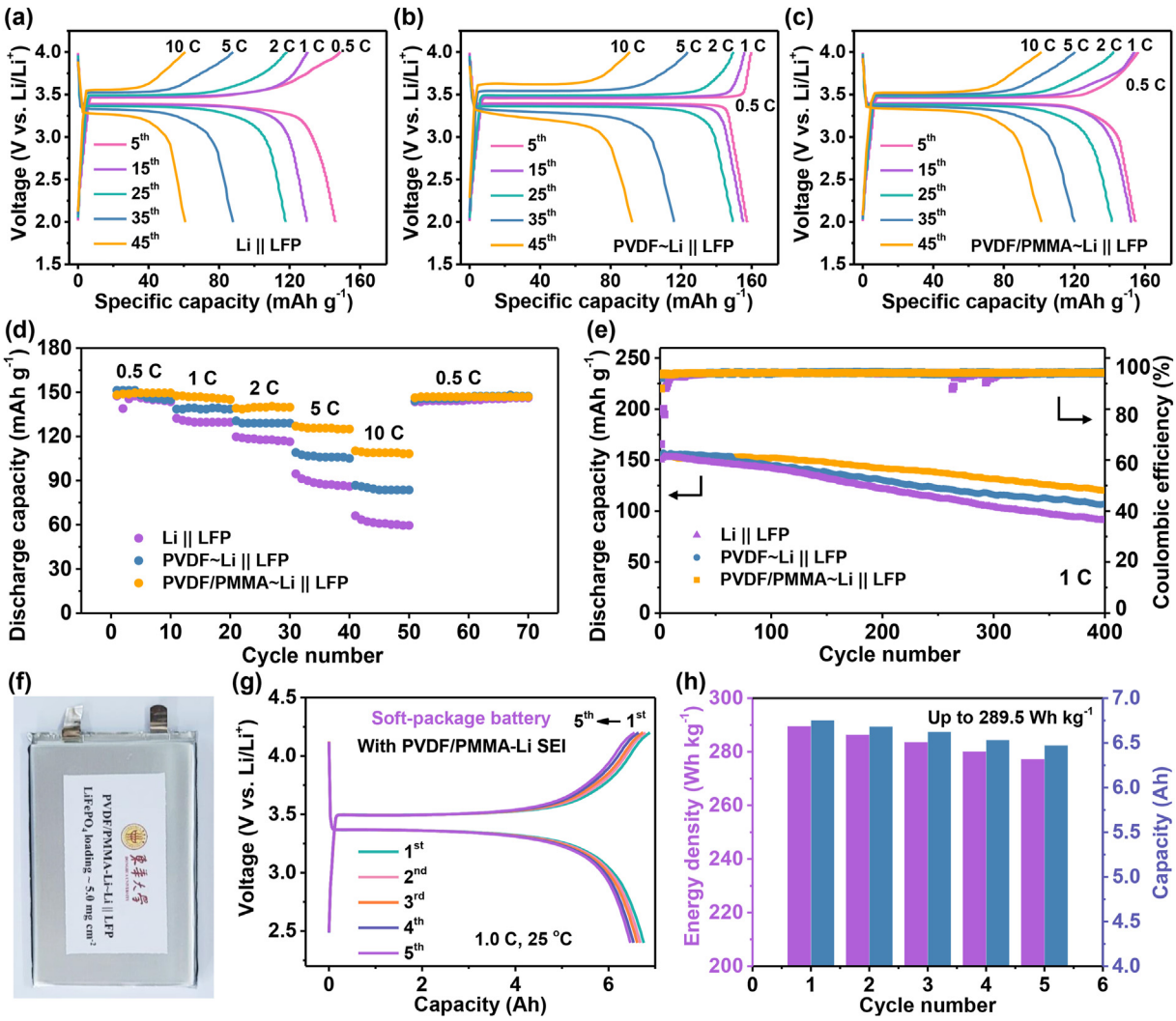

Fig. 6. Voltage profiles of the full cells (a) without interlayer, and with (b) PVDF and (c) PVDF/PMMA interlayers. (d) Rate performance and (e) capacity retention of Li || LFP batteries without or with different interlayers. (f) Digital photograph of the 10 Ah PVDF/PMMA ~ Li || LFP soft-package cell. (g) Capacity profiles of the 10 Ah soft-package PVDF/PMMA ~ Li || LFP battery, and (h) the corresponding energy density (violet) and capacity (blue) values after different cycles.

A $LiFePO_4$(LFP) cathode was employed to assemble full cells, which consisted of 80 wt% LFP powder, 10 wt% conductive additive (Super P), and 10 wt% organic binder (PVDF). The areal loading of the LFP in the cathodes of the coin cell was ~5 mg cm^{-2}. The soft-package PVDF/PMMA-Li || LFP batteries were assembled using an MSK-115-III in an argon-filled glove-box. Celgard 2400 was used as a separator, and 2 g A h^{-1} of 1 M lithium bis(trifluoromethanesulfonyl)imide (LiTFSI) in 1,3-dioxolane (DOL) and dimethoxymethane (DME) (v:v, 1:1) with 2% $LiNO_3$ additive was employed as the electrolyte. To increase the energy density of the soft-package battery, the thickness of the cathode was pressed to ~100 μm with a roller. Typically, the cathode area was fixed around 46.75 cm^2 (8.5 cm × 5.5 cm), and the average LFP mass loading was ~15 mg cm^{-2} (2.55 mAh cm^{-2}). It is worth noting that the battery cathodes were double-coated with LFP. The Li metal foils (33 μm in thickness) were purchased from China Energy Lithium Co., Ltd. and pressed to 20 μm with a roller. The charge/discharge tests were performed on a NEWARE CT-4800T-5V6A-S1 multichannel battery tester. All electrochemical tests were carried out at room temperature (25 °C).

4.5. Simulation

The theoretical DFT calculations for a simplified fragment of PVDF, which was Bis(vinylidene fluoride) ($C_4H_6F_4$), with Li^+ were obtained for different distances between the Li^+ and the polar functional C–F groups. In comparison, the theoretical calculations for a simplified fragment of PMMA-Li (i.e., Bis(methyl methacrylate), $C_{16}H_{22}O_4Li_4$) and Cu atom were conducted to absorb Li^+ at 25 °C. The adsorption energy of the structure was calculated using the Vienna Ab initio Simulation Package (VASP). The lithium metal deposition process was performed using the "Electrodeposition, Tertiary Nernst-Planck" module of COMSOL Multiphysics 5.6. All the models were set with Li metal and an electrolyte, as shown in Fig. S8. The white circles in Fig. S8b represent the PVDF fibers, while the cyan layer between the PVDF fibers and the Cu foil acted as the PMMA-Li-derived SEI in Fig. S8c. According to the electrochemical impedance spectra of the full cells based on the above models (Fig. S24), the diffusion coefficient of Li^+ in the electrolyte with PVDF fibers was set at 0.5 × 10^{-9} m^2 s^{-1}, and the diffusion coefficient with the PMMA-Li-derived SEI was 6.49 times higher, at 3.25 × 10^{-9} m^2 s^{-1}. The initial concentration of Li^+ in the electrolyte was kept at 1 M. The detailed parameters in the simulation process are provided in Table S4.

Author contributions

The article was written through contributions from all the authors, all of whom have approved the final version of the manuscript.

Declaration of competing interest

The authors declare that they have no known competing financial interests or personal relationships that could have appeared to influence the work reported in this paper.

Acknowledgments

The authors are grateful for the financial support from the National Natural Science Foundation of China (22075042), the Natural Science Foundation of Shanghai (20ZR1401400), the Fundamental Research Funds for the Central Universities, and the Donghua University (DHU) Distinguished Young Professor Program (LZB2021002).

Appendix B. Supplementary data

Supplementary data to this article can be found online at https://doi.org/10.1016/j.esci.2022.02.003.

References

[1] S. Wei, S. Choudhury, Z. Tu, K. Zhang, L.A. Archer, Electrochemical interphases for high-energy storage using reactive metal anodes, Acc. Chem. Res. 51 (2018) 80–88.
[2] K. Fu, Y. Li, M. Dirican, C. Chen, Y. Lu, J. Zhu, Y. Li, L. Cao, P.D. Bradford, X. Zhang, Sulfur gradient-distributed CNF composite: a self-inhibiting cathode for binder-free lithium–sulfur batteries, Chem. Commun. 50 (2014) 10277–10280.
[3] J.B. Goodenough, K.S. Park, The li-ion rechargeable battery: a perspective, J. Am. Chem. Soc. 135 (2013) 1167–1176.
[4] D. Lin, Y. Liu, Y. Cui, Reviving the lithium metal anode for high-energy batteries, Nat. Nanotechnol. 12 (2017) 194–206.
[5] J. Luo, C.C. Fang, N.L. Wu, High polarity poly(vinylidene difluoride) thin coating for dendrite-free and high-performance lithium metal anodes, Adv. Energy Mater. 8 (2018) 1701482.
[6] H.J. Peng, J.Q. Huang, X.B. Cheng, Q. Zhang, Review on high-loading and high-energy lithium-sulfur batteries, Adv. Energy Mater. 7 (2017) 1700260.
[7] S. Xin, Y. You, S. Wang, H.C. Gao, Y.X. Yin, Y.G. Guo, Solid-state lithium metal batteries promoted by nanotechnology: progress and prospects, ACS Energy Lett. 2 (2017) 1385–1394.
[8] E. Peled, Advanced model for solid electrolyte interphase electrodes in liquid and polymer electrolytes, J. Electrochem. Soc. 144 (1997) 208.
[9] Y. Guo, H. Li, T. Zhai, Reviving lithium-metal anodes for next-generation high-energy batteries, Adv. Mater. 29 (2017) 1700007.
[10] D. Lu, Y. Shao, T. Lozano, W.D. Bennett, G.L. Graff, B. Polzin, J. Zhang, M.H. Engelhard, N.T. Saenz, W.A. Henderson, P. Bhattacharya, J. Liu, J. Xiao, Failure mechanism for fast-charged lithium metal batteries with liquid electrolytes, Adv. Energy Mater. 5 (2015) 1400993.
[11] K. Zhang, G.H. Lee, M. Park, W. Li, Y.M. Kang, Recent developments of the lithium metal anode for rechargeable non-aqueous batteries, Adv. Energy Mater. 6 (2016) 1600811.
[12] C. Yang, K. Fu, Y. Zhang, E. Hitz, L. Hu, Protected lithium-metal anodes in batteries: from liquid to solid, Adv. Mater. 29 (2017) 1701169.
[13] F. Wu, Y.X. Yuan, X.B. Cheng, Y. Bai, Y. Li, C. Wu, Q. Zhang, Perspectives for restraining harsh lithium dendrite growth: towards robust lithium metal anodes, Energy Storage Mater. 15 (2018) 148–170.
[14] C. Yan, P. Zhu, H. Jia, J. Zhu, R.K. Selvan, Y. Li, X. Dong, Z. Du, I. Angunawela, N. Wu, M. Dirican, X. Zhang, High-performance 3-D fiber network composite electrolyte enabled with li-ion conducting nanofibers and amorphous PEO-based cross-linked polymer for ambient all-solid-state lithium-metal batteries, Adv. Fiber Mater. 1 (2019) 46–60.
[15] H. Kim, G. Jeong, Y.U. Kim, J.H. Kim, C.M. Park, H.J. Sohn, Metallic anodes for next generation secondary batteries, Chem. Soc. Rev. 42 (2013) 9011.
[16] S. Shiraishi, Surface condition changes in lithium metal deposited in nonaqueous electrolyte containing HF by dissolution-deposition Cycles, J. Electrochem. Soc. 146 (1999) 1633.
[17] J. Zhao, L. Liao, F. Shi, T. Lei, G. Chen, A. Pei, J. Sun, K. Yan, G. Zhou, J. Xie, C. Liu, Y. Li, Z. Liang, Z. Bao, Y. Cui, Surface fluorination of reactive battery anode materials for enhanced stability, J. Am. Chem. Soc. 139 (2017) 11550–11558.
[18] W. Li, H. Yao, K. Yan, G. Zheng, Z. Liang, Y.M. Chiang, Y. Cui, The synergetic effect of lithium polysulfide and lithium nitrate to prevent lithium dendrite growth, Nat. Commun. 6 (2015) 7436.
[19] L. Suo, Y.S. Hu, H. Li, M. Armand, L. Chen, A new class of solvent-in-salt electrolyte for high-energy rechargeable metallic lithium batteries, Nat. Commun. 4 (2013) 1481.
[20] F. Ding, W. Xu, G.L. Graff, J. Zhang, M.L. Sushko, X. Chen, Y. Shao, M.H. Engelhard, Z. Nie, J. Xiao, X. Liu, P.V. Sushko, J. Liu, J.G. Zhang, Dendrite-free lithium deposition via self-healing electrostatic shield mechanism, J. Am. Chem. Soc. 135 (2013) 4450–4456.
[21] Y.J. Gong, J.W. Heo, H. Lee, H. Kim, J. Cho, S. Pyo, H. Yun, H. Kim, S.Y. Park, J. Yoo, Y.S. Kim, Nonwoven rGO fiber-aramid separator for high-speed charging and discharging of li metal anode, Adv. Energy Mater. 10 (2020) 2001479.
[22] J. Liu, R. Xu, C. Yan, H. Yuan, J.F. Ding, Y. Xiao, T.Q. Yuan, J.Q. Huang, In situ regulated solid electrolyte interphase via reactive separators for highly efficient lithium metal batteries, Energy Storage Mater. 30 (2020) 27–33.
[23] Y. Luo, T. Li, H. Zhang, Y. Yu, A. Hussain, J. Yan, H. Zhang, X. Li, New insights into the formation of silicon-oxygen layer on lithium metal anode via in situ reaction with tetraethoxysilane, J. Energy Chem. 56 (2021) 14–22.
[24] Y. Chen, G. Zhou, W. Zong, Y. Ouyang, K. Chen, Y. Lv, Y.E. Miao, T. Liu, Porous polymer composite separators with three-dimensional ion-selective nanochannels for high-performance Li–S batteries, Compos. Commun. 25 (2021) 100679.
[25] C. Zhou, W. Zong, G. Zhou, X. Fan, Y.E. Miao, Radical-functionalized polymer nanofiber composite separator for ultra-stable dendritic-free lithium metal batteries, Compos. Commun. 25 (2021) 100696.
[26] M. Hu, Y. Yuan, M. Guo, Y. Pan, D. Long, A substrate-influenced three-dimensional unoriented dispersion pathway for dendrite-free lithium metal anodes, J. Mater. Chem. 6 (2018) 14910–14918.
[27] K. Yan, H.W. Lee, T. Gao, G. Zheng, H. Yao, H. Wang, Z. Lu, Y. Zhou, Z. Liang, Z. Liu, S. Chu, Y. Cui, Ultrathin two-dimensional atomic crystals as stable interfacial layer for improvement of lithium metal anode, Nano Lett. 14 (2014) 6016–6022.
[28] J. Qian, Y. Li, M. Zhang, R. Luo, F. Wang, Y. Ye, Y. Xing, W. Li, W. Qu, L. Wang, L. Li, Y. Li, F. Wu, R. Chen, Protecting lithium/sodium metal anode with metal-organic framework based compact and robust shield, Nano Energy 60 (2019) 866–874.
[29] Y. Guo, Y. Ouyang, D. Li, Y. Wei, T. Zhai, H. Li, PMMA-assisted Li deposition towards 3D continuous dendrite-free lithium anode, Energy Storage Mater. 16 (2019) 203–211.
[30] Z. Zhou, Y. Feng, J. Wang, B. Liang, Y. Li, Z. Song, D.M. Itkis, J. Song, A robust, highly stretchable ion-conducive skin for stable lithium metal batteries, Chem. Eng. J. 396 (2020) 125254.
[31] H. Zhang, X. Liao, Y. Guan, Y. Xiang, M. Li, W. Zhang, X. Zhu, H. Ming, L. Lu, J. Qiu, Y. Huang, G. Cao, Y. Yang, L. Mai, Y. Zhao, H. Zhang, Lithiophilic-lithiophobic gradient interfacial layer for a highly stable lithium metal anode, Nat. Commun. 9 (2018) 3729.
[32] S. Huang, L. Tang, H.S. Najafabadi, S. Chen, Z. Ren, A highly flexible semi-tubular carbon film for stable lithium metal anodes in high-performance batteries, Nano Energy 38 (2017) 504–509.
[33] N. Li, W. Wei, K. Xie, J. Tan, L. Zhang, X. Luo, K. Yuan, Q. Song, H. Li, C. Shen, E.M. Ryan, L. Liu, B. Wei, Suppressing dendritic lithium formation using porous media in lithium metal-based batteries, Nano Lett. 18 (2018) 2067–2073.
[34] Z. Liang, G. Zheng, C. Liu, N. Liu, W. Li, K. Yan, H. Yao, P.C. Hsu, S. Chu, Y. Cui, Polymer nanofiber-guided uniform lithium deposition for battery electrodes, Nano Lett. 15 (2015) 2910–2916.
[35] J. Hu, P. He, B. Zhang, B. Wang, L.Z. Fan, Porous film host-derived 3D composite polymer electrolyte for high-voltage solid state lithium batteries, Energy Storage Mater. 26 (2020) 283–289.
[36] D. Lin, Y. Liu, W. Chen, G. Zhou, K. Liu, B. Dunn, Y. Cui, Conformal lithium fluoride protection layer on three-dimensional lithium by nonhazardous gaseous reagent freon, Nano Lett. 17 (2017) 3731–3737.
[37] J.L. Ma, Y.B. Yin, T. Liu, X.B. Zhang, J.M. Yan, Q. Jiang, Suppressing sodium dendrites by multifunctional polyvinylidene fluoride (PVDF) interlayers with nonthrough pores and high flux/affinity of sodium ions toward long cycle life sodium oxygen-batteries, Adv. Funct. Mater. 28 (2018) 1703931.
[38] Z. Zhou, Y. Feng, J. Wang, B. Liang, Y. Li, Z. Song, D.M. Itkis, J. Song, A robust, highly stretchable ion-conducive skin for stable lithium metal batteries, Chem. Eng. J. 396 (2020) 125254.
[39] M. Worzakowska, TG/FTIR/QMS studies of long chain esters of geraniol, J. Anal. Appl. Pyrol. 110 (2014) 181–193.
[40] C. Lievens, D. Mourant, M. He, R. Gunawan, X. Li, C.Z. Li, An FT-IR spectroscopic study of carbonyl functionalities in bio-oils, Fuel 90 (2011) 3417–3423.
[41] B.C. Shekar, S. Sathish, R. Sengoden, Spin coated nano scale PMMA films for organic thin film transistors, Phys. Procedia 49 (2013) 145–157.
[42] Y. Wang, L. Zhang, L. Zhang, F. Zhang, P. He, H. Zheng, H. Zhou, Reversible lithium-ion uptake in poly(methylmethacrylate) thin-film via lithiation/delithiation at in situ formed intramolecular cyclopentanedione, Adv. Energy Mater. 6 (2016) 1601375.
[43] V.H. Pham, T.T. Dang, S.H. Hur, E.J. Kim, J.S. Chung, Highly conductive poly(methyl methacrylate) (PMMA)-reduced graphene oxide composite prepared by self-assembly of PMMA latex and graphene oxide through electrostatic interaction, ACS Appl. Mater. Interfaces 4 (2012) 2630–2636.
[44] J.M. Montero, M.A. Isaacs, A.F. Lee, J.M. Lynam, K. Wilson, The surface chemistry of nanocrystalline MgO catalysts for FAME production: an in situ XPS study of H_2O, CH_3OH and CH_3OAc adsorption, Surf. Sci. 646 (2016) 170–178.
[45] I.O. Ucar, M.D. Doganci, C.E. Cansoy, H.Y. Erbil, I. Avramova, S. Suzer, Combined XPS and contact angle studies of ethylene vinyl acetate and polyvinyl acetate blends, Appl. Surf. Sci. 257 (2011) 9587–9594.
[46] H. Ju, X. Feng, Y. Ye, L. Zhang, H. Pan, C.T. Campbell, J. Zhu, Ca carboxylate formation at the calcium/poly(methyl methacrylate) interface, J. Phys. Chem. C 116 (2012) 20465–20471.
[47] D.A. Shirley, High-resolution X-ray photoemission spectrum of the valence bands of gold, Phys. Rev. B 5 (1972) 4709–4714.